Opto-Electronic Science

CN 51-1800/O4 ISSN 2097-0382 (Print) ISSN 2097-4000 (Online)

Smart photonic wristband for pulse wave monitoring

Renfei Kuang, Zhuo Wang, Lin Ma, Heng Wang, Qingming Chen, Arnaldo Leal Junior, Santosh Kumar, Xiaoli Li, Carlos Marques and Rui Min

Citation: Kuang RF, Wang Z, Ma L, et al. Smart photonic wristband for pulse wave monitoring. *Opto-Electron Sci* **3**, 240009 (2024).

https://doi.org/10.29026/oes.2024.240009

Received: 21 February 2024; Accepted: 12 June 2024; Published online: 20 August 2024

Related articles

Spatiotemporal hemodynamic monitoring via configurable skin-like microfiber Bragg grating group

Hengtian Zhu, Junxian Luo, Qing Dai, Shugeng Zhu, Huan Yang, Kanghu Zhou, Liuwei Zhan, Biao Xu, Ye Chen, Yanqing Lu, Fei Xu

Opto-Electronic Advances 2023 **6**, 230018 doi: 10.29026/oea.2023.230018

Progress on infrared and terahertz electro-magnetic absorptive metasurface

Deng Honglang, Zhou Shaolin, Cen Guanting

Opto-Electronic Engineering 2019 **46**, 180666 doi: 10.12086/oee.2019.180666

Development of a hybrid photoacoustic and optical monitoring system for the study of laser ablation processes upon the removal of encrustation from stonework

Athanasia Papanikolaou, George J. Tserevelakis, Kristalia Melessanaki, Costas Fotakis, Giannis Zacharakis, Paraskevi Pouli

Opto-Electronic Advances 2020 **3**, 190037 doi: 10.29026/oea.2020.190037

Intelligent metaphotonics empowered by machine learning

Sergey Krasikov, Aaron Tranter, Andrey Bogdanov, Yuri Kivshar

Opto-Electronic Advances 2022 **5**, 210147 doi: 10.29026/oea.2022.210147

More related article in Opto-Electronic Journals Group website

Opto-Electronic Science

http://www.oejournal.org/oes

OE_Journal

Website

Opto-Electronic Science

Article

December 2024, Vol. 3, No. 12

DOI: 10.29026/oes.2024.240009

Smart photonic wristband for pulse wave monitoring

Renfei Kuang[1,3], Zhuo Wang[1], Lin Ma[2], Heng Wang[2], Qingming Chen[3], Arnaldo Leal Junior[4], Santosh Kumar[5], Xiaoli Li[1], Carlos Marques[6] and Rui Min[1*]

Real-time acquisition of human pulse signals in daily life is clinically important for cardiovascular disease monitoring and diagnosis. Here, we propose a smart photonic wristband for pulse signal monitoring based on speckle pattern analysis with a polymer optical fiber (POF) integrated into a sports wristband. Several different speckle pattern processing algorithms and POFs with different core diameters were evaluated. The results indicated that the smart photonic wristband had a high signal-to-noise ratio and low latency, with the measurement error controlled at approximately 3.7%. This optimized pulse signal could be used for further medical diagnosis and was capable of objectively monitoring subtle pulse signal changes, such as the pulse waveform at different positions of Cunkou and pulse waveforms before and after exercise. With the assistance of artificial intelligence (AI), functions such as gesture recognition have been realized through the established prediction model by processing pulse signals, in which the recognition accuracy reaches 95%. Our AI-assisted smart photonic wristband has potential applications for clinical treatment of cardiovascular diseases and home monitoring, paving the way for medical Internet of Things-enabled smart systems.

Keywords: smart healthcare; specklegram; pulse monitoring; gesture recognition; artificial intelligence; wearable sensor

Kuang RF, Wang Z, Ma L et al. Smart photonic wristband for pulse wave monitoring. *Opto-Electron Sci* **3**, 240009 (2024).

Introduction

Cardiovascular disease, particularly stroke and ischemic heart disease, has become the leading cause of death in the world, with the number expected to rise to 23.6 million per year by 2030[1]. Despite such a high mortality rate from cardiovascular diseases, most of them[2], such as hypertension, coronary heart disease, myocardial infarction, and atherosclerosis, can be prevented and treated through pre-diagnosis in conjunction with daily monitoring of physiologic signals. Conventional health monitoring systems are flawed in terms of wearability, portability, and intelligence, and are failing to collect clinical-grade personal vital indicators for health diagnosis in daily life[3]. The need for affordable and comfortable biomedical devices for continuous monitoring continues to be a significant barrier to promoting the utility of intelligent systems like Internet of Things-enabled

[1]Center for Cognition and Neuroergonomics, State Key Laboratory of Cognitive Neuroscience and Learning, Beijing Normal University, Zhuhai 519087, China; [2]College of Science, Shenyang Aerospace University, Shenyang 110136, China; [3]School of Microelectronics Science and Technology, Guangdong Provincial Key Laboratory of Optoelectronic Information Processing Chips and Systems, Sun Yat-Sen University, Zhuhai 519082, China; [4]Graduate Program in Electrical Engineering, Federal University of Espírito Santo, Fernando Ferrari Avenue, Vitoria 29075-910, Brazil; [5]Department of Electronics and Communication Engineering, Koneru Lakshmaiah Education Foundation, Vaddeswaram, Andhra Pradesh 522302, India; [6]CICECO-Aveiro Institute of Materials, Physics Department, University of Aveiro, Aveiro 3810-193, Portugal.
*Correspondence: R Min, E-mail: ruimin@bnu.edu.cn

Received: 21 February 2024; Accepted: 12 June 2024; Published online: 20 August 2024

technology in healthcare monitoring. Pulse waves are a prominent component of physiological signaling and involve abundant health information that can reveal individual conditions, including heart problems (such as arrhythmia), blood pressure, pulse wave velocity, exercise, sleep status, and so on[4–6]. Real-time monitoring of pulse signals and effective medical analysis are of clinical significance for the monitoring and diagnosis of the cardiovascular system[7–9].

In addition to diagnosing fundamental diseases, the more in-depth analysis of pulse waves plays an active role in various fields, including multi-location monitoring to aid in traditional Chinese medicine diagnosis, and gesture recognition. For thousands of years, traditional Chinese medicine has utilized the pulse wave to predict and prevent diseases in their early stages. Empirical approaches have been proposed to analyze the physical state of pulse waves, rendering pulse wave surveillance indispensable for this practice. However, traditional Chinese medicine is unable to continuously monitor pulse waves, limiting the accuracy of the assessment results[10]. On the other hand, it is well known that gesture recognition provides a broad arena for the development of advanced areas such as human-computer interaction and intelligent medical robotics[11]. With the innovation of artificial intelligence (AI), IoT, and 5G/6G technologies, electronic sensors based on different detection principles have been developed and used for obtaining data on pulse waves[12]. Currently, various types of electronic wearable sensors are used to acquire the pulse signal, including piezoelectric[13–15], resistance[16–18], and capacitance[19–21]. These sensors have received widespread attention for their ability to monitor pulse signals in a non-invasive manner for efficient, rapid, and accurate diagnosis of cardiovascular diseases. However, electromagnetic interference, a narrow linear-time response interval, lack of wearability, and safety issues restrict the practical applications of electronic sensors to some extent[4].

In recent years, optical fiber sensing and optical communication network technologies have experienced rapid development[22], and different optical fiber sensing technologies have been successfully applied in various application fields. Optical fiber sensors provide a promising alternative to electronic sensors due to their distinct advantages of sensitivity, linearity, resistance to drift, inherent electric safety, and electromagnetic interference immunity. However, poor electromagnetic compatibility of some electrical medical sensors leads them cannot be used in specific medical settings that demand resistance to electromagnetic interference. Consequently, one of the reasons we chose optical fibers in pulse monitoring devices is their immunity to electromagnetic disturbances. Several recent studies have focused on monitoring pulse waves based on optical fiber sensors. Wang et al.[23] developed an ultrasensitive, flexible optical fiber sensor with a fast response time based on a polydimethylsiloxane-encapsulated microfiber coupler. Additionally, fiber Bragg gratings (FBGs) have been utilized to detect pulse waves at various peripheral pulsatile sites, including the brachial, radial, and carotid arteries, on several body parts, such as the finger, elbow, and wrist[24,25]. Moreover, optical fiber sensors are compatible with fabric fibers, making them suitable for incorporation into fabrics (e.g., wristbands), and improving wearing comfort in a manner that is not feasible compared with wearable electrical sensors. Li, et al. demonstrated the first example of a fully integrated optical interrogator, which was integrated with a wristband, enabling the detection of body temperature and heart sounds[26]. Li, et al. proposed a fiber-optic wearable wristband system based on fiber end-faces coated with polydimethylsiloxane (PDMS) + Ag composite diaphragms for continuous pulse waveform measurements[27]. Recent advancements in wearable optical fiber sensors allow for comfortable and conformal integration with the human body. Nevertheless, the optical fiber sensors reported above still face challenges as wearable devices due to the weak physiological signals from the body surface.

Fiber specklegram sensors (FSSs) have significant advantages in meeting the above requirements. FSSs are a type of optical fiber sensor based on the multimode interference effect and have been developed rapidly in the past few years due to advantages such as high sensitivity, high precision, and fast response[28–32]. Herein, the details of the pulse waveform can be distinguished to estimate the pulse rate more accurately. Bennett et al.[33] designed a sensing system in which a silica multimode optical fiber was placed on the wrist and chest to accomplish simultaneous measurement of heart rate and pulse rate. However, silica optical fiber may cause damage to the body in some specific sensing scenarios, such as wearable devices, due to some disadvantages of the sensors based on silica optical fiber, such as low flexibility and fragmentation ability[34]. Therefore, sensors with high flexibility and low-cost demodulation are necessary for physiological

signal monitoring. Polymer optical fibers (POFs) are made of polymer materials such as polymethyl methacrylate (PMMA)[35], TOPAS (a cyclic olefin copolymer)[36], ZEONEX (cyclo-olefin polymer)[37] and CYTOP (amorphous fluoropolymers)[38] with the advantages of low-cost, high flexibility, strain limits, fracture toughness, and a low Young's modulus[39–41]. Therefore, the sensor based on POF is one promising solution for pulse signal monitoring, which can be attempted as a suitable alternative to traditional methods and fulfill the requirements of further clinical trials.

In this work, we analyze multimode optical fiber speckle images for wrist pulse obtained by embedding a POF sensor in a sports wristband as a smart photonic wristband. POFs with different core diameters and various image-processing algorithms were designed to optimize the sensor, and finally, combined with artificial intelligence algorithms, a low-cost and high-precision AI-assisted pulse-monitoring device was obtained. Compared to other existing works, the smart photonic wristband present here has improved sensitivity, accuracy, and portability and the collected pulse signal contained detailed medical information, enabling pulse palpation measurements similar to those made by well-trained practitioners of traditional Chinese medicine, including the identification of pulse indicators such as the pulse positions of Cun, Guan, and Chi. Additionally, the different gestures can be recognized from the acquired pulse wave signals utilizing convolutional neural network (CNN) processing, achieving a 95% accuracy rate. A smartphone visual monitoring system was also developed for personalized medicine, providing customers with a user-friendly experience and facilitating the advancement of medical cloud IoT technology. Our proposed smart photonic wristband integrated by POFs forms real wearable "fabric sensors" that will drive the development of smart photonic textiles and change daily life in the area of medical IoT. The proposed sensor offers an approach to visual diagnosis that integrates both Eastern and Western medical practices, advancing the standardization and objectification of traditional pulse diagnostic techniques. The convergence of these two diagnostic methods enables cross-verification of information, thereby increasing the accuracy of diagnoses.

Experimental procedure

Speckle pattern and system design

When the laser is coupled into a multimode optical fiber, speckle patterns are formed at the output end of the optical fiber, showing a granular pattern that is generated by interference between conduction modes during transmission. The far-field light speckle distribution is the coherent superposition of all mode amplitudes, as shown in Eq. (1):

$$A(x,y) = \sum_{m=0}^{M} a_m(x,y)\exp\left[\mathrm{j}(\varphi_m(x,y)\right], \qquad (1)$$

where $a_m(x,y)$ and $\varphi_m(x,y)$ are the amplitude and phase distributions of the m-th mode. The far-field speckle pattern intensity $I(x, y)$ captured by the CMOS camera can be described as:

$$I(x,y) = \sum_{m=0}^{M}\sum_{n=0}^{M} a_m(x,y)a_n(x,y) \cdot \exp\left[\mathrm{j}(\varphi_m(x,y) - \varphi_n(x,y))\right], \qquad (2)$$

where a_m and a_n, φ_m and φ_n are the amplitude and phase of the m-th and n-th modes on pixel (x, y), respectively. In addition, the deformation of the fibers causes perturbations in the propagation medium of each mode, which in turn affects the variation of the speckle pattern image. When the fibers are subjected to a physical disturbance, such as a pulse, these important physiological signs can be determined by tracking and processing the intensity of the speckle pattern.

The experimental setup shown in Fig. 1 consists of three main parts: the signal-generating device, the POF-based smart photonic wristband, and the specklegram processing part. The optical signal generated from a benchtop laser (THORLABS, S1FC660, 650 nm) is delivered to the POF with a multimode silica optical fiber (50/125 μm). In the experiment, the employed POF was the commercially available Mitsubishi QY40-2.2E optical fiber, which is made of polymethyl methacrylate (PMMA) with the advantages of high flexibility, strain limits, fracture toughness, and a low Young's modulus. A sports wristband incorporates the POF sensing part into a smart photonic wristband through sewing and embedding. To enhance sensitivity, Fig. 1(c) sets the POF-based smart photonic wristband design into three circles. The pulse disturbs the POF close to the wrist, causing a change in the speckle pattern.

The specklegram processing part consists of an industrial camera (Hikvision MV-CA013-AOUM, USB3.0) and a computer equipped with MATLAB (R2020b). The defocus camera captures the output speckle pattern, which will be analyzed by the MATLAB program to obtain the desired pulse signal. The settings of the CMOS

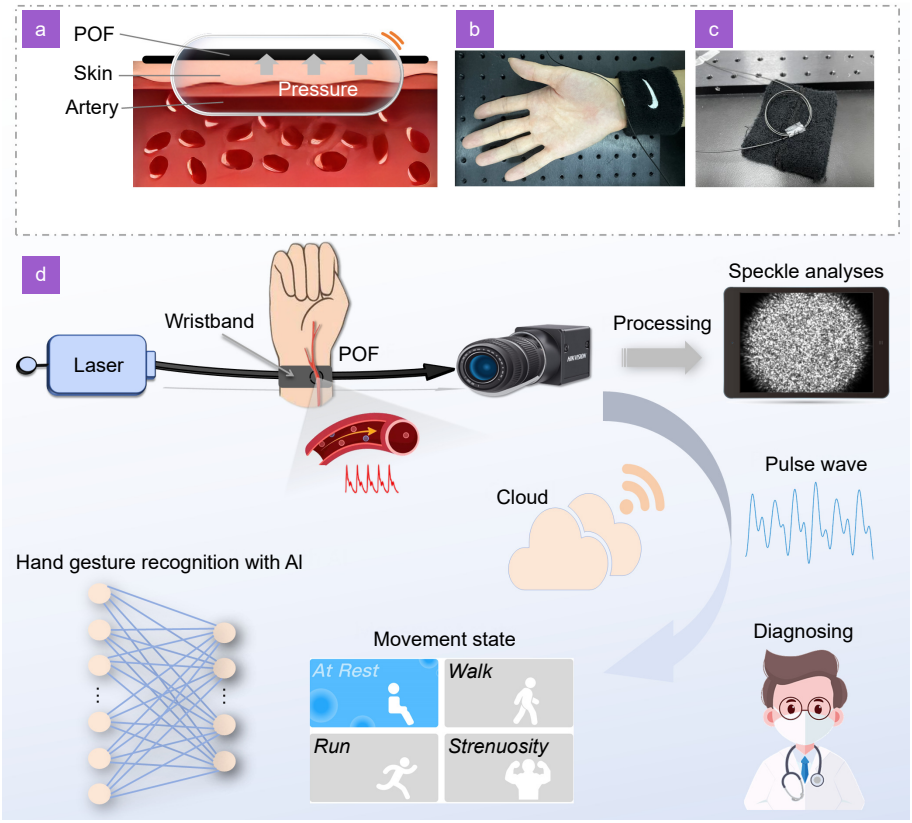

Fig. 1 | Schematic diagram of the overall design. The diagram illustrates (**a**) the sensing principle of the smart photonic wristband. (**b**) The physical view of the wristband POF-based sensor. (**c**) The internal structure of the sensor. (**d**) The monitoring system, which includes a laser (light source), POF wristband sensor, signal acquisition, data processing, pulse rate computation, cloud terminal, and an artificial intelligence processor.

webcam determine the sensitivity and accuracy of the sensing, as shown in Table 1. In terms of image acquisition hardware, there is still room to further optimize, such as using industrial CMOS sensors with smartphones or portable cameras to facilitate the development of cost-effective, portable monitoring devices.

Specklegram processing

The overall procedure for processing speckle patterns is presented in Fig. 2, where the changes in speckle patterns are detected by the CMOS webcam. A video is captured by the webcam during the experiment. The video is output frame-by-frame, and then each frame is masked to implement the image-denoising operation. The specific procedure is to initially set a threshold value and then return all pixel values below the threshold value to zero. Subsequently, the video is output frame-by-frame, and then color-to-grayscale processing is performed on each frame.

The wrist pulse is applied to the sensing area of the smart photonic wristband, resulting in changes in the transmission light field inside the POF. Specifically, the mode coupling effect occurs with the change in amplitude in Eq. (2), which were causes the distribution of the speckle field to change with the external perturbation. Moreover, for the phase change, the real-time speckle field intensity $I(x, y, k)$ can be compared with the reference speckle field intensity $I_o(x, y)$ to estimate the phase deviation, where k is the discrete-time value representing the intensity frame. Once mode-coupling and phase modulation occur in the POF, the speckle pattern changes and is shown as the change in the gray value of each pixel in the image. The variation in a sequence of speckle patterns is shown in Fig. 2 and which caused by

Table 1 | Some webcam parameters of the video recording process.

Exposure type	Video frame rate	Focal length	Video resolution	Sensor area
Global shutter	30 FPS	12 mm	1280×1024	1/2"

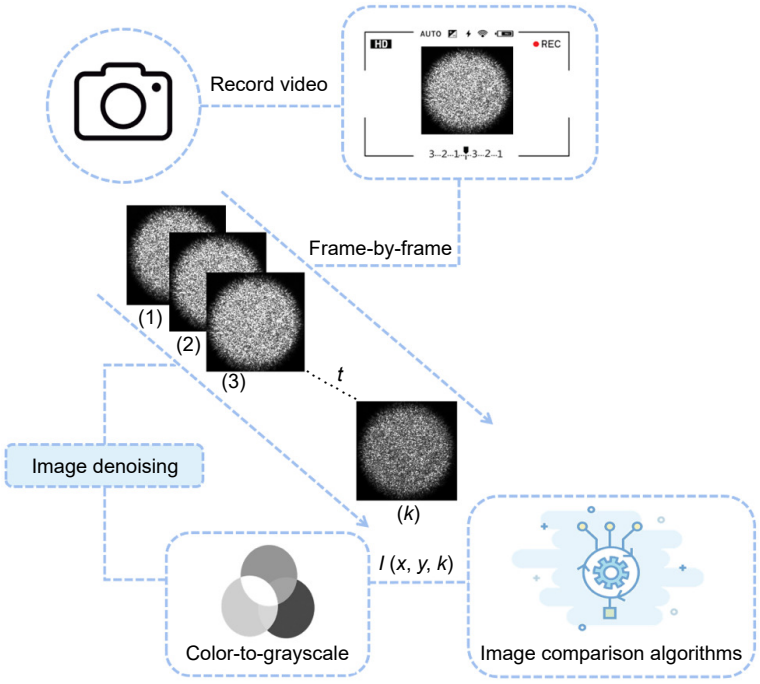

Fig. 2 | Scheme of the specklegram image processing. The middle block diagram shows an example of the frame-to-frame difference under external continuous disturbances.

consecutive external perturbations. The corresponding image processing algorithm can be used to track the speckle field modulation caused by any effect. A simple differential image processing method is employed to obtain a one-dimensional pixel intensity signal. Specifically, the overall speckle patterns are analyzed, and the change information in the speckle patterns is extracted by calculating the difference in the intensity of all $M\times N$ pixel points in two speckles between frames, which is defined as follows:

$$I_{\mathrm{DM}}(i)=\frac{1}{M\cdot N}\sum_{x}^{M}\sum_{y}^{N}\left|I_k(x,y)-I_1(x,y)\right|\ , \qquad (3)$$

where M and N represent the number of rows and columns in the speckle pattern, respectively, and $I_k(x,y)$ corresponds to the pixel value of the coordinates (x,y) in the k-th frame speckle image.

Data analysis

In this section, the pulse rate can be extracted by analyzing the specific area of one spectrum image. The direct-current (DC) component of the data is eliminated, and the power spectrum of optical power is calculated by using Welch' s overlapped segment averaging estimator[42]. The proposed processing steps for extracting the pulse rate are as follows:

Firstly, the pulse wave signal is divided into segments as shown in Eq. (4):

$$x_i(n)=x(n+iM-M)\,,\ 0\le n<M,\ 1\le i<L \qquad (4)$$

where M is the window length, L is the number of data sample segments, and i is the number of each segment. Then, Eq. (5) is used to calculate the modified periodograms of each segment in a Hamming window design.

$$I_i(\omega)=\frac{1}{U}\left|\sum_{n=0}^{M-1}x_i(n)\,w(n)\exp(-\mathrm{j}\omega n)\right|^2,$$
$$i=1,2\ldots,M-1,\ \text{with}\ U=\frac{1}{M}\sum_{n=0}^{M-1}w^2(n)\ , \qquad (5)$$

where $I_i(\omega)$ is the periodogram of each segment, $w(n)$ refers to the window function in symmetric Hamming design[43], ω is the frequency, and j is the imaginary unit. Then, the power spectrum of the signal is obtained by superposition and averaging according to Eq. (6).

$$P_x(\mathrm{e}^{\mathrm{j}}\omega)=\frac{1}{L}\sum_{i=1}^{L}I_i(\omega)\ . \qquad (6)$$

The data are passed through a bandpass filter that corresponds to the frequency range of the pulse (frequency band of 0.8–2.5 Hz) to determine the exact pulse rate.

Results and discussion

Wrist pulse signal monitoring

To obtain accurate pulse signals, a smart photonic wristband protocol has been implemented for the test. Participants were asked to wear the smart photonic

wristband on the wrist comfortably, keeping the sensing area in direct contact with the skin near the carpal artery (see Fig. 1). The optical fiber surround provides a large sensing area, while the angle and distance worn on the wrist allow for minimal fitting error. Considering the real-time variations of the pulse signal, the video is recorded along four 30 s segments for a total of 2 minutes. The results of pulse wave signal detection by the smart photonic wristband are shown in Fig. 3(a), and the pulse wave time series for 30 s are shown in Fig. 3(a-I), where the amplitude and frequency of the pulse wave are unstable. Additionally, the frequency range of the signal indicates that the pulse signal cannot be clearly distinguished, as shown in Fig. 3(a-II). To improve the accuracy and efficiency of monitoring, further investigations are supplied here.

From the previous study, we concluded that differential image processing methods are not sufficient to obtain desirable results, and selecting an optimal algorithm to address the speckle field modulation is critical for obtaining an effective pulsed signal. Several algorithms for processing speckle patterns are depicted in Fig. 4, which are widely used in literature to characterize the degree of images. These methods are introduced in detail in the supplementary information, which are mainly selected based on two different categories: NIPC, ZNCC, FM, and GLCM are correlation methods, MI and SSD are difference methods.

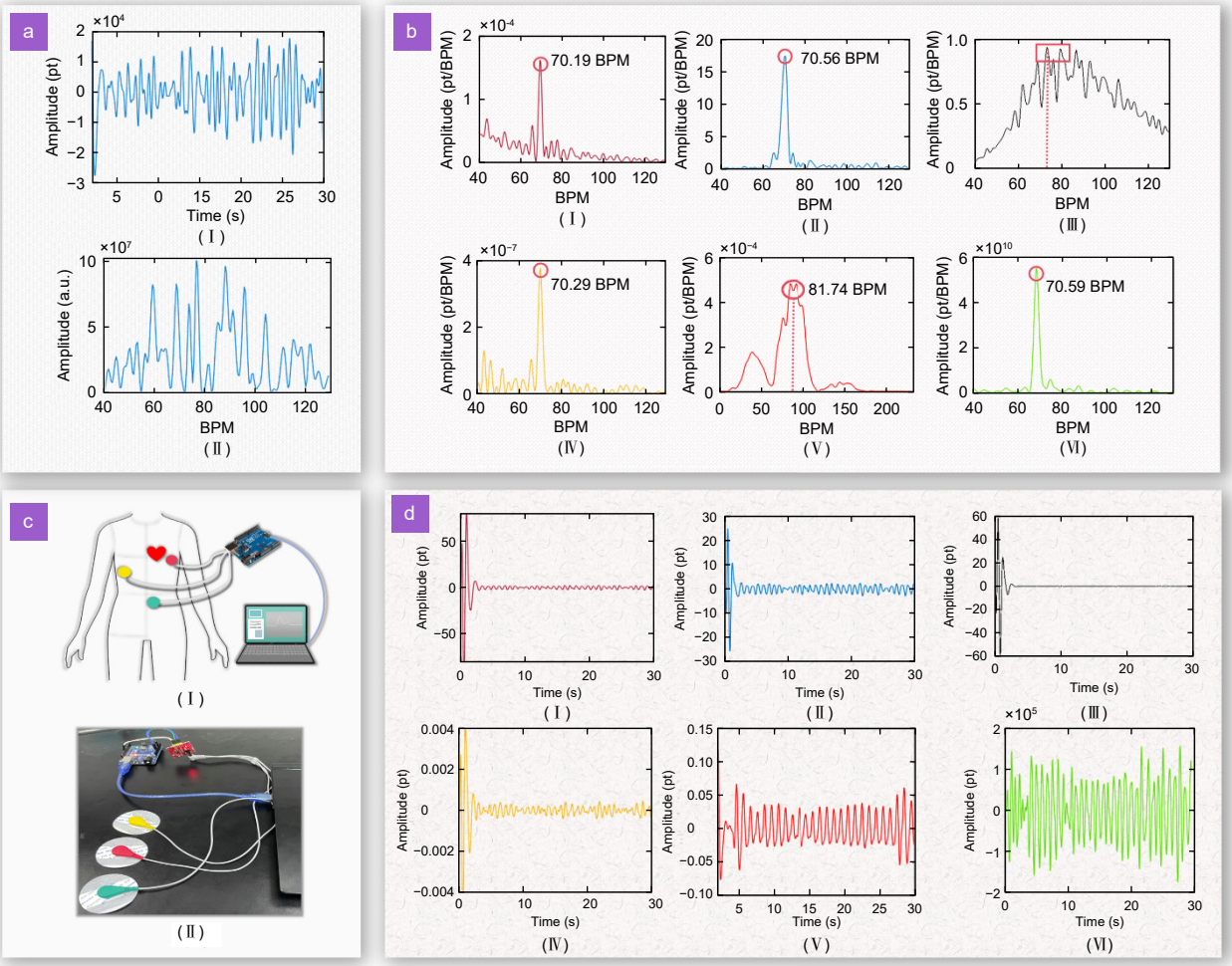

Fig. 3 | Performance testing and optimization of the smart photonic wristband. (**a**) Results of a preliminary experiment: (I) Time-domain response of human pulse signal; (II) Power spectral density corresponding to the pulse signal. (**b**) Pulse waveforms from different processing methods. The method names corresponding to subscripts (I) to (VI) are normalized inner-product coefficient, zero-mean normalized cross-correlation, first-order moment, gray-level co-occurrence matrix, mutual information, and the sum of squared differences, respectively. (**c**) ECG reference signal acquisition device. (I) Schematic diagram; (II) Actual photograph. (**d**) Signal response in the frequency spectrum of different processing methods. The method names corresponding to subscripts (I) to (VI) are normalized inner-product coefficient, zero-mean normalized cross-correlation, first-order moment, gray-level co-occurrence matrix, mutual information, and the sum of squared differences, respectively.

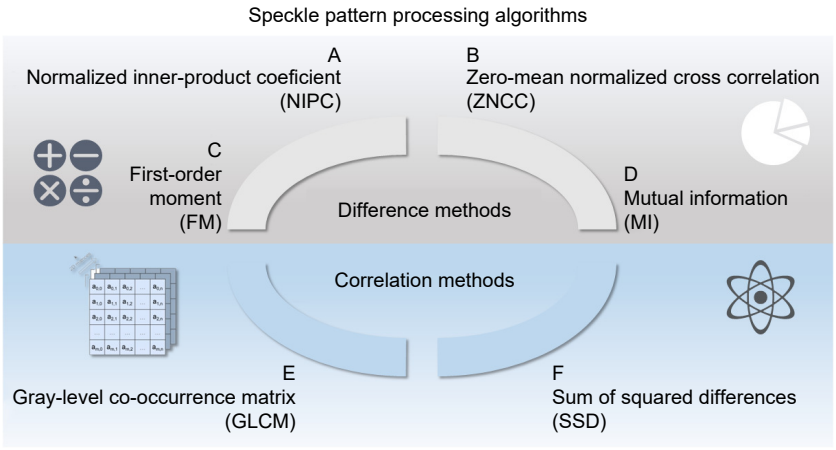

Fig. 4 | Processing algorithms for speckle patterns using various methods.

Optimization of the speckle processing methods

Based on the discussion algorithms above, although the individual algorithms work differently, the ultimate goal is to obtain one-dimensional spectral pixel intensities that carry the information of the speckle pattern variations. To evaluate the performance of image processing algorithms in pulse signal monitoring, different metrics have been measured. Similar procedures in previous section have been followed for subsequent experiments, the experiment results in the time domain with different image processing methods (Fig. 3(d)), whereas the other parameters have been kept identical to previous measurements. The signal response in the frequency spectrum is obtained as shown in Fig. 3(b), and the pulse rate is depicted as the beats per minute (BPM). The ordinate in the figure corresponds to the relative amplitude after Fourier transforms, and the abscissa corresponding to the peak value is the monitored pulse rate in BPM.

As illustrated in Fig. 3(d-I/II), the poor amplitude stability of the time domain signal in the first few seconds affects the overall waveform observation and prevents further processing and diagnosis. The results indicate that the NIPC/ZNCC method is more suitable for processing linear, regular, and large amplitude speckle intensity changes[44]. Moreover, compared to the NIPC method, the ZNCC method accounts for the mean value of the pixel intensities in the collected speckle images under the same conditions, causing the calculation results to be more robust. Thus, as shown in Fig. 3(d-IV), the amplitude of the pulse wave calculated by the ZNCC method is two orders of magnitude larger than that of the NIPC method. In addition, from Fig. 3(b-I/II), the processing effect of low-frequency noise signals below 1 Hz (60 BPM) with the ZNCC method is significantly better than that of the NIPC method.

Here, the first-order moment algorithm uses the concept of mathematical expectation to address the correlation function, which is not practical for pulse monitoring. According to Fig. 3(d-III), there is almost no change in the waveform, and it is unable to detect the weak vibration. In addition, the performance evaluation of the MI algorithm is complicated because the process of converting the pixel intensity to an image entropy loses information about each pixel.

Moreover, the accuracy and time complexity of those algorithms are the key factors affecting the monitoring effect. The difference between the pulse rate obtained from the smart photonic wristband and the heart rate measured by a standard electrocardiographic device (AD 8232) is recorded[45]. Normally, the pulse rate and heart rate are consistent[46]. We prefer ECG to PPG as the reference standard because ECG signals are generally more accurate than PPG signals[47], and PPG signal acquisition inherently involves measurement errors. The subjects were asked to wear the smart photonic wristband at the wrist for data collection, and three ECG electrodes were attached to the chest and abdomen as required to monitor the reference signals. The diagram of the reference monitoring signal acquisition is shown in Fig. 3(c), where the subject pulse signal was simultaneously measured with the reference signal. Table 2 shows the pulse rates of participants who were monitored in different states and the measurements were repeated three times in each state to assess the accuracy and specificity of the algorithm in determining the pulse rate. As presented in Table 2, the response indicates an error of less than 5.3%

Table 2 | Summary of test pulse rate results for different algorithms.

Algorithms		NIPC	ZNCC	FM	GLDM	MI	SSD	Reference
Pulse rate (BPM)	No. 1	71.19±3.5	70.56±1.2	/	70.29±4.2	81.74±4.4	70.59±1.8	74.22±2.5
	No. 2	63.22±2.0	62.87±1.8	/	64.19±3.7	69.95±3.9	62.08±1.1	65.17±1.9
	No. 3	78.92±2.5	78.37±1.9	/	77.12±3.0	/	78.07±0.9	80.69±2.3
	No. 4	57.61±1.7	57.02±2.0	/	56.89±3.3	63.13±2.8	56.32±1.3	58.61±1.7
	No. 5	95.05±5.2	95.44±4.9	/	92.54±8.1	/	96.50±5.7	98.76±7.2
Computation time (s)		113.16±1.2	111.63±1.3	125.77±8.0	87.42±2.7	5056.71±79.3	92.10±0.5	/

for the pulse rate measurements. FM and MI methods failed to measure the pulse rate, but the other algorithms were effective in measuring the pulse signals.

Based on the processing time, the different methods can complete the calculation of a 30 s video within 100 s, which is better than the correlation method. The GLDM method is the fastest due to use the of MATLAB's built-in function to directly measure the image gray values for computation, which is highly encapsulated. The MI method initially calculates the gray entropy and then translates it into the form of a mutual information function with a long processing time. As shown in Fig. 3(d-VI), the sum of the squared differences method successfully demodulated the frequency information of the pulse vibration signal from the sensing curve. Due to the SSD processing two adjacent frames, the results obtained are better than the differential image processing method (see Fig. 3(b-II)). In contrast, the differential image processing method selects the first frame of the video as a fixed reference state, which creates uncertainty, reduces the dynamic range of algorithm processing, and is suitable for most algorithms, such as the NIPC and the ZNCC method. Therefore, compared with other algorithms, the SSD method is simple to implement and shows high sensitivity to intensity variations, as presented in Fig. 3(d-VI). The signal response in the frequency spectrum (see Fig. 3(b-VI)) also reflects optimal monitoring; the main noise outside of 60–80 BPM (1–1.33 Hz) filtered out, showing a clear pulse signal that is suitable for further discussion.

Optimization of the smart photonic wristband

As mentioned above, the SSD method is one of the differential methods, and the sensitivity of the smart photonic wristband processed by the differential methods is provided by the amount and contrast of speckles in the captured images[48]. Moreover, the amount of speckle formation due to mode interference depends on the propagation conditions of the optical fiber; thus, the sensitivity can be enhanced by appropriately adjusting the core diameter of the multimode optical fiber. To determine the performance of the sensors with different core diameters, POFs with core diameters of 250/500/750/1000 μm were selected and evaluated. The experimental conditions were the same as previously, and each video was recorded along six 30 s segments, totaling 3 minutes, corresponding to the different types of POFs. In the speckle patterns, as shown in Fig. 5(a), the number of speckles was proportional to the core diameter of the POF, which was the same as the theoretical result[49].

The pulse signals detectable by the four types of POFs were discussed, and the corresponding smart photonic wristbands are anticipated to undergo further optimization studies. Reference signals were still obtained from the standard ECG device. The reference ECG signal with the detected T-waves and the acquired pulse signal collected from the POF with a core diameter of 500 μm are illustrated in Fig. 5(b). The T-wave peak was easily located in the ECG signal, which corresponded to the percussion wave peaks of the pulse signal. The time difference between the two peaks corresponded to the time delay, and the mean values and the standard deviations of delays are depicted in Fig. 5(c). The results indicated that the time delay error measured by POFs of different sizes had a slight difference, with an average of 231.5±42.5 ms and a standard deviation of 21.0 ms.

A comparison of the pulse power spectrum measured by different POFs indicates that a greater speckle number in the image correlates to a higher peak value of the dominant frequency of the signal power spectrum (see Fig. 5(d)). When the area captured by the image is constant, the smaller the speckle, the more susceptible the optical power intensity is to external changes. For the selected core diameters (250–1000 μm), the corresponding POF sensors were capable of receiving a sufficient number of speckles and were sensitive enough for pulse rate monitoring in the frequency domain. However, the

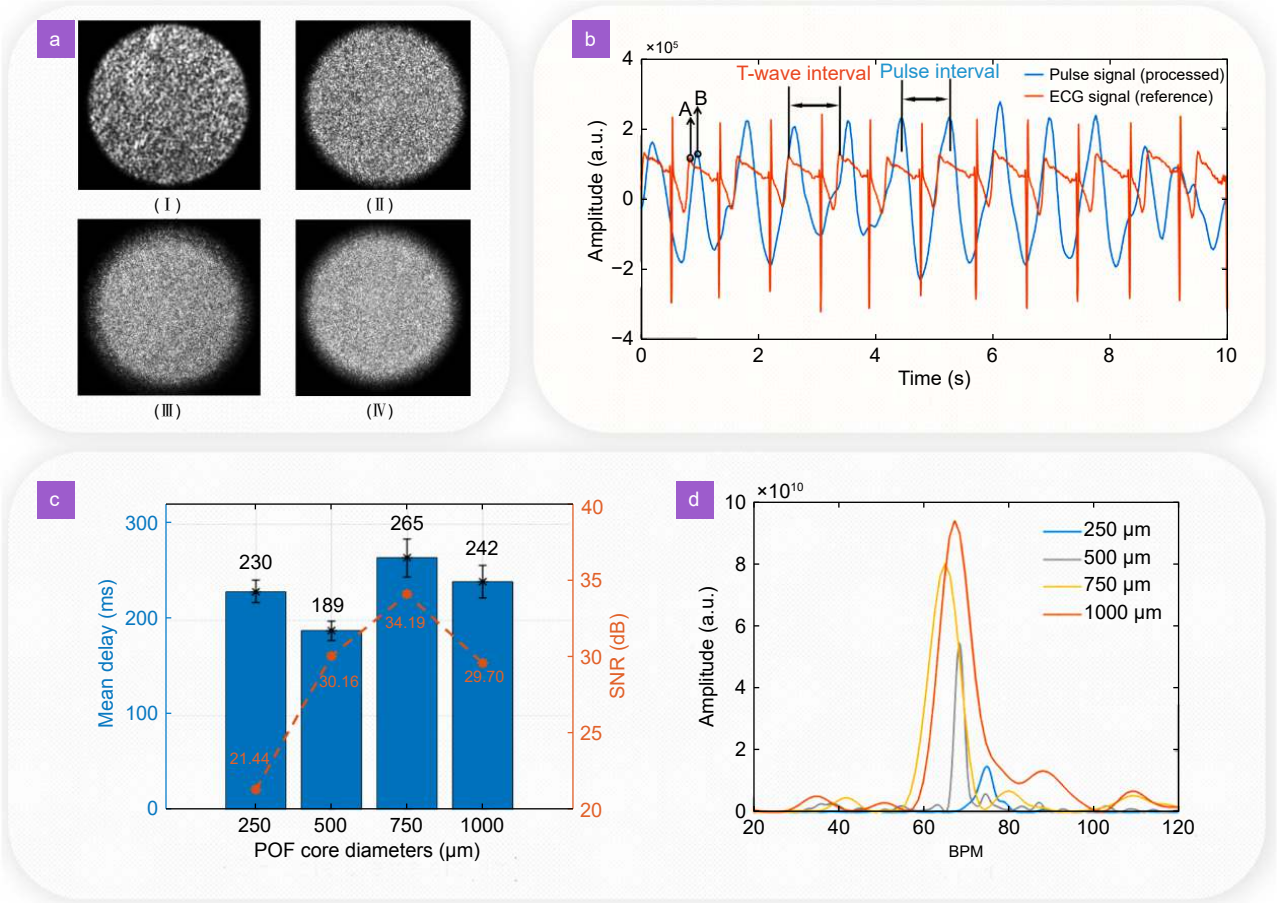

Fig. 5 | (**a**) Speckle images formed by the POFs with different core diameters: (I) 250 μm; (II) 500 μm; (III) 750 μm; (VI) 1000 μm. (**b**) Example of a 10-s long comparison between a processed signal and a reference signal, where A is the T-wave peak in the ECG signal and B is the percussion-wave peak in the pulse signal. (**c**) Some results of the tested different core diameters, where the left ordinate is the time delay and the right ordinate is the SNR. (**d**) Signal response in the frequency domain with the different core diameters.

situation appears different for pulse wave signals in the time domain. The signal-to-noise ratio (SNR) of the image is interpreted as the ratio of the effective pulse signal to the power spectrum of the noise and varies for the different core diameters. The average value of the power spectrum in the stationary state is defined as the image noise. When the core diameter of the POF exceeds a certain value, the pulse wave signal has some burr noise and the sensing effect deteriorates. As shown in Fig. 5(c), the experimental results indicate that the POF with a 750 μm core diameter has the best SNR.

Specifically, four different core diameters of POF exhibited similar response times (231.5±42.5 ms). In the frequency domain, the 750 μm core diameter POF demonstrated a distinctly clear and significant pulse rate, with an intensity slightly lower than that of the 1000 μm core diameter POF, which also possessed the highest signal-to-noise ratio (SNR) at 34.19 dB. In the time domain, the 750 μm core diameter POF not only captured the dicrotic wave but also achieved a noise reduction. Hence, the 750 μm core diameter POF was selected for optimization. The pulse wave obtained after the optimization of the POF core diameter is shown in Fig. 6(a), where t_0 represents a complete pulse wave. Each cycle of the waveform is associated with a pulse, and the peaks and valleys represent the diastole and systole of the radial artery, respectively. Some specific information in the pulse wave can be obtained, as illustrated in Fig. 6(a-II). A complete pulse wave contains information, such as intensity, trend, shape, width, and rhythm variation. The display of this detailed information is capable of helping the follow-up medical diagnosis, such as the strength of the pulse and the monitoring of pulse wave abnormalities.

Subsequently, the bending and indentation tests were implemented to evaluate the mechanical and optical properties of the POF. The POF was installed on a

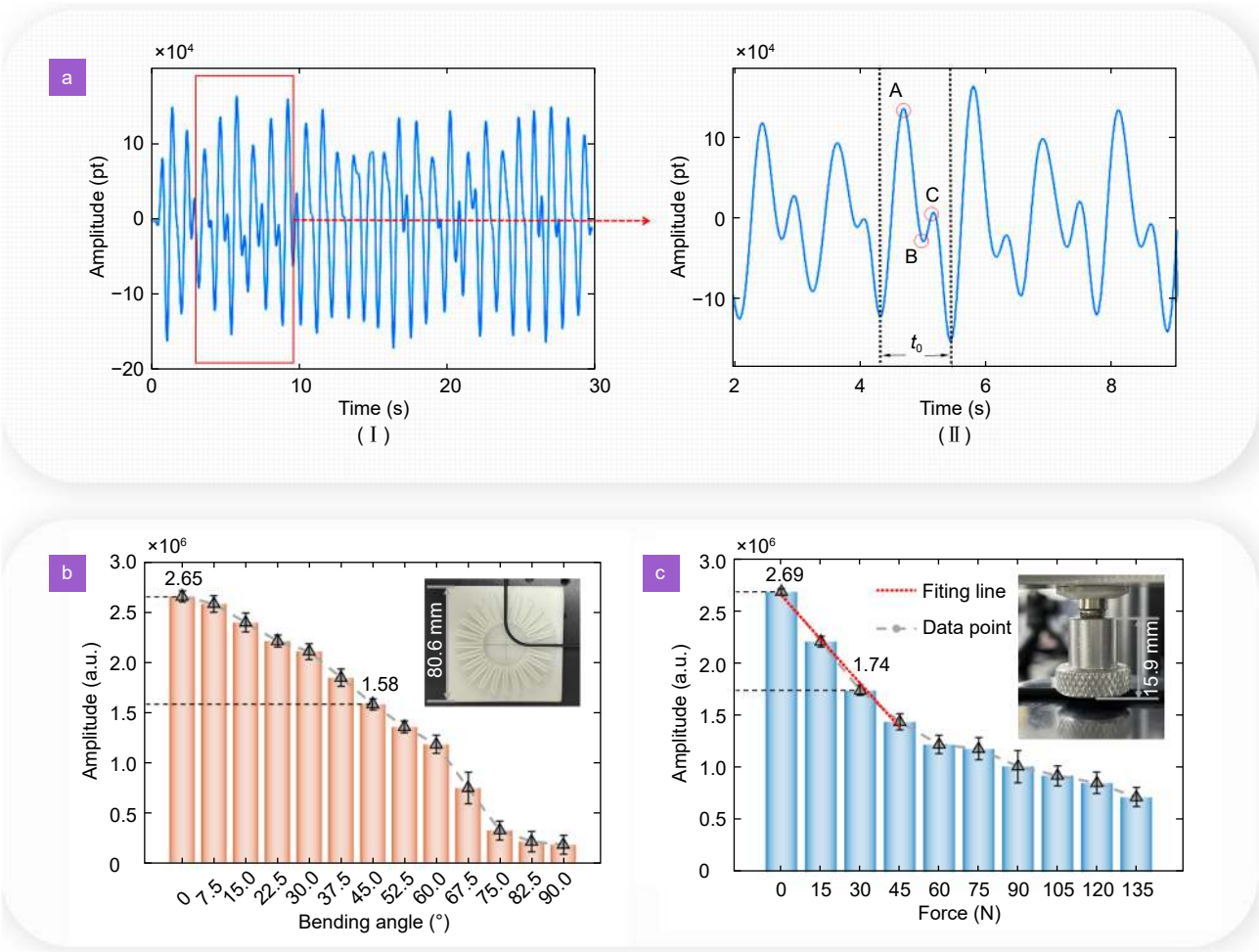

Fig. 6 | (**a**) (I) Human pulse signal diagram acquired under the optimal method; (II) Detail within 10 s; A is the percussion wave (PW), B is the dicrotic notch, and C is the dicrotic wave. (**b**) Optical power-pressure curves of POF sensors in indentation tests. (**c**) Relationship between optical power and bending radius of POF sensor in bending tests.

homemade broad with various bending angles, as illustrated in the inset of Fig. 6(b). Subsequently, measured the speckle pattern's power spectral intensity under different bending radii. The POF was bent from a straight state to a preset bending angle and then returned to the straight state. The power spectral intensity of the speckle pattern was measured on average after 50 cycles. As shown in Fig. 6(b), the power spectral intensity through the POF decreases as the bending angle increases. Notably, when the bending angle increased from 0 to 45 degrees (forming a loop), the optical power intensity decreased from 2.65×10⁶ (pt) to 1.58×10⁶ (pt), and about 60% of the light could pass through the POF. Furthermore, to assess the mechanical performance under bending conditions, pressure tests were performed on the POF with a force gauge (HANDPI, HP-500), as depicted in the inset of Fig. 6(c). Specifically, pressures ranging from 0 to 135 N were applied in 15 N increments on one side of the POF, with each pressure value measured 20 times. When the applied pressure exceeded 150 N, repeated applications resulted in POF damage. The resulting pressure-speckle pattern power spectral intensity curve, as shown in Fig. 6(c), indicates the POF exhibited a decreasing light power curve under applied pressure, with a linear working range of 0–45 N. A high linearity (R^2 = 0.989) was demonstrated within this range, which helps to avoid distortion in pulse wave signal detection. The experimental results indicated that the optical power intensity decreases from 2.69×10⁶ (pt) to 1.74×10⁶ (pt) as the pressure increases from 0 to 30 N. Under a pressure of 30 N, the POF could still transmit about 65% of the light, demonstrating its strong resistance to lateral pressure. These results indicate the POF not only has high stability and excellent durability but also ensures that the light signal sensitively varies with shape changes during bending or pressure variations.

So far, an optimal method suitable for long-term detection is proposed, where the sensing part of the POF is configured as three loops in the smart photonic wristband. The speckle pattern information was collected using the SSD algorithm, while the 750 μm core diameter POF was selected for the experiment. The distribution of the specklegram signal power over the frequency domain was extracted using the power spectral density (PSD) method to determine the pulse rate. Four healthy subjects were subsequently selected for testing, and the results of the performance analysis are shown in Table 3.

Averaging the performance results in Table 3 results in a monitoring error of 3.7%, a processing time consumption of 93.67 s, a signal-to-noise ratio of 34.96 dB, and a measurement delay of 269.9 ms.

Multiposition pulse monitoring

The Cunkou diagnostic method is one of the most common methods of pulse collection in the clinical diagnosis of traditional Chinese medicine (TCM). Practitioners can determine the physiological and pathological state of the body by feeling the pulse beating at the Cunkou. The Cunkou normally includes three special positions, namely, Cun (distal), Guan (middle), and Chi (proximal). The medial part of the radial styloid process is marked as Guan, the anterior part of Guan (wrist side) is Chi, and the posterior part of Guan (elbow side) is Cun, the schematics of these three positions are shown in Fig. 7(a-I).

Thus, based on the TCM, the smart photonic wristband was placed at three different Cunkou locations (Cun, Guan, and Chi) for further analysis. The pulse was continuously monitored by adjusting the position of the smart photonic wristband, as shown in Fig. 7(a-I), and changing the position at 30-s intervals, repeating each position five times. The pulse wave signals corresponding to the three sensing locations are recorded, as depicted in Fig. 7(a-II). The pulse rates are collected continuously at these three locations and show essentially the same value of 73 beats per minute. The experimental results indicate that the characteristic peaks of the pulse waveforms at different Cunkou positions can be identified; the pulse amplitude at the Guan position is the largest, the pulse amplitude at the other two positions is similar, and the Cun position is slightly larger. Six healthy college students (three males and three females) were selected to repeat the test, and the results indicate our wristband obtained a pulse across various Cunkou locations with good repeatability performance. Significantly, in the TCM diagnosis, changes in the pulse collected at different positions of Cunkou can also determine the effect of pathogeny on the internal organs[50]. The radial artery's three positions correspond to the meridians and internal organs, as shown in Table 4.

However, despite its frequent use in clinical practice, pulse diagnosis has been criticized and questioned by Western physicians due to its lack of mathematical and physical characteristics. Our wristband sensor offers TCM practitioners visualized information about pulse signals at the Cun, Guan, and Chi positions, enabling the interpretation of wrist pulse physical parameters from both qualitative and quantitative perspectives[51], such as the oscillation frequency, intensity, length, and width of the pulse. Consequently, in the future, it will be of great significance to develop this kind of wristband for multi-location monitoring of health conditions and diseases.

Experimentally, the effect of different user movement states on sensing is evaluated. The smart photonic wristband was attached to the wrist artery of a 22-year-old healthy female volunteer to collect pulse signals. The pulse signal was first recorded while the volunteer was at rest. The volunteer was then asked to perform an open-close jump exercise at a rate of 50 times per minute (see Fig. 7(b-I)). Immediately after the exercise, the pulse signal is detected by the smart photonic wristband. Figure 7(b-II) shows the changes in the wrist pulse wave signal at rest, after 2 min of exercise, and after 4 min of exercise, where the pulse rates were 58, 75, and 102 per minute, respectively.

In summary, sustained high-intensity exercise results in an increase in pulse rate and a larger pulse amplitude. Additionally, the smart photonic wristband can capture subtle variations in the pulse waveform before and after

Table 3 | Optimized smart photonic wristband response with different subjects.

Subjects	Our sensor (BPM)	Reference (BPM)	Error	Time-consuming (s)	SNR (dB)	Delay (ms)
1	62.0±2.3	64.8±1.0	4.52%	93.23±0.76	34.92±2.89	251.5±5.2
2	79.5±2.2	82.1±3.6	3.17%	92.19±3.05	37.05±4.16	259.2±8.0
3	66.6±3.5	70.2±4.1	5.13%	93.20±1.92	32.21±7.52	302.0±10.6
4	75.8±1.6	77.3±3.3	1.94%	96.06±1.19	35.63±3.05	267.2±4.8

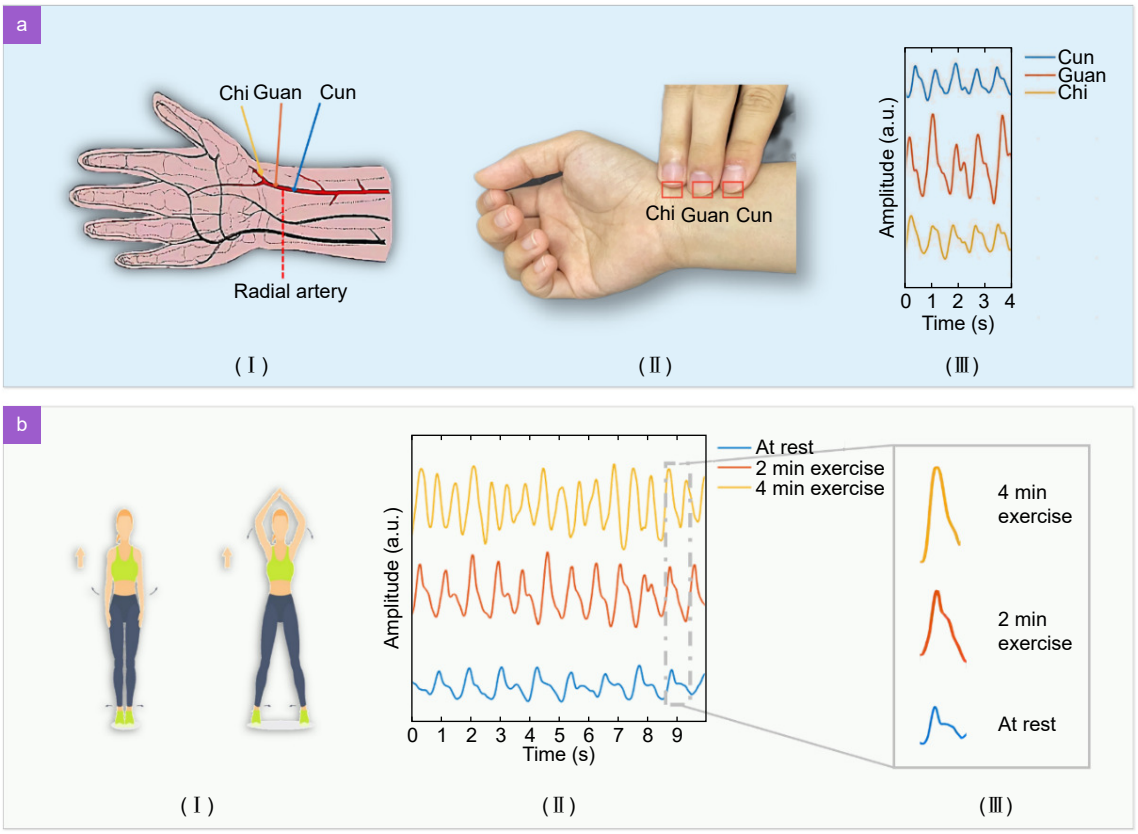

Fig. 7 | (**a**) Diagnostic method of the Cunkou illustration. (I) Schematic illustrating the position of Cunkou. (II) Pulse waveforms at different positions of Cun, Guan, and Chi. (**b**) Pulse monitoring pre- and post-exercise. (I) Exercise example schematic. (II) Pulse waveforms at different exercise durations. (III) Waveform details in different states.

Table 4 | The correspondence of the Cun, Guan and Chi with the organs of the body.

Position	Cun	Guan	Chi
Left arterial wrist	Heart	Liver & Gallbladder	Kidney
Right arterial wrist	Lung & Chest	Stomach	Kidney

exercise. One complete pulse wave cycle for different exercise states is extracted, as depicted in Fig. 7(b-III). After 4 minutes of exercise, the percussion wave peak significantly increases, and the dicrotic wave becomes irregular with a tendency to be blurry. These results indicate that sustained high-intensity exercise over a short period leads to significant changes in the pulsed signal, consistent with phenomena observed in previous clinical studies.

Hand gesture recognition with AI

Gestures may provide a significant amount of data, so precise recognition of these movements is crucial for enhancing the effectiveness and functionality of human-computer interaction technology. Various gestures induce distinct muscle actions, likely giving rise to different signal responses by the smart photonic wristband, which in turn affects the waveform changes of the wrist pulse wave. Hence, an experiment was devised to investigate the ability of the smart photonic wristband to detect changes in gestures. Participants were recorded holding five different gestures for three minutes. Using the feature extraction algorithms mentioned in the supplement, pulse wave signals were obtained that corresponded to each of the different gestures. To classify the gestures, we utilized machine learning algorithms, which can effectively achieve regression and classification. To enhance model classification accuracy, three feature extraction algorithms, the NIPC method, the ZNCC method, and the differential image processing method, are selected to create a three-dimensional eigenvalue time series data signal, and 160 sample groups are acquired frame by frame. Following the random arrangement of the samples, 120

groups of samples were implemented for training, and 40 groups for testing.

Subsequently, a three-layer, one-dimensional convolutional neural network to extract deep features from signals to clearly characterize the classification results of different gestures was designed. Then, the data is unfolded and fed to the fully connected layer for classification. The specific network model is depicted in Fig. 8(a). After multiple iterations, a classification model is obtained. Finally, 20 datasets were used to evaluate the predictive ability of the model and the results are represented using a confusion matrix. As illustrated in Fig. 8(b), with the assistance of the convolutional neural network, different gestures have been distinguished, achieving a classification accuracy of 95%. These results indicate that smart photonic wristbands are promising for applications to assist in healthcare strategy development and future human-computer interactions by recognizing changes in gestures.

Visualisation of the smartphone interface

The internet of things (IoT) is an emerging technology that has shown great promise in recent years. The healthcare sector has high expectations for IoT technology due to the synergy between the market demand for health monitoring and the development of IoT technology. Over the past decade, the healthcare internet of things (H-IoT) has demonstrated its potential application in connecting various medical devices, sensors, and healthcare professionals to deliver high-quality medical services. A wearable health monitoring system combined with the H-IoT will be a promising alternative to traditional healthcare systems. Hence, one cloud-based system was implemented for data processing. The computer connected to the CMOS camera acquires the user's pulse signal, and the data is interconnected using Wi-Fi to the cloud. Ultimately, the data is processed in the cloud to obtain the user's physiological information and then transmitted to a smartphone.

When clicking the "START PULSE MONITORING" button in Fig. 9, each frame of the speckle plot can be sent to the IoT system via the Bluetooth device. After collecting the data, the measurement results can be visible in the smartphone application. Transferring cloud data in this way has the problem of uploading data too slowly, which still requires a solution in the future. As illustrated in Fig. 9, the pulse rate (64 BPM), possible movement state (at rest), and health assessment (in comparison to other users) obtained from the smart photonic wristband are displayed on the mobile application, allowing the user to see their current health state quickly. Ultimately, users can easily share their health parameter data with their doctors instantly within our application and seek health counseling and medical assistance when needed. Elderly patients, patients with arrhythmias, and patients with coronary heart disease (CHD) will be able to keep their health under control over time with the help of the cloud system developed. By visualizing the smartphone interface, we are truly enabling wearable healthcare by integrating fiber optic sensors into body area networks.

Conclusions

To conclude, we propose a speckle pattern analysis based POF sensor integrated with a wristband for pulse signal monitoring as a smart photonic wristband. The smart photonic wristband present here has advantages such as simple operation, low-cost, and good performance for

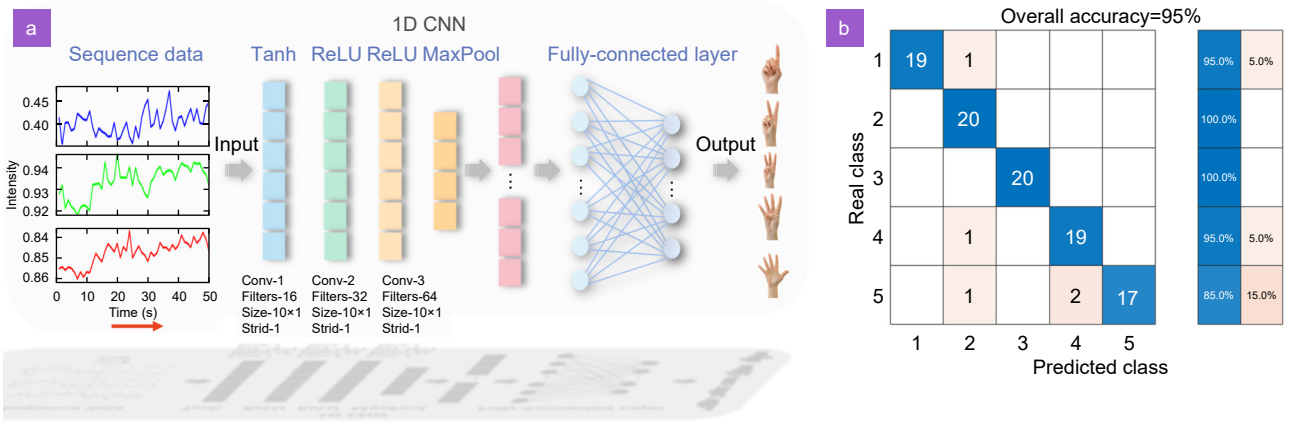

Fig. 8 | Flowchart of the neural network model and classification results. (**a**) Neural network processing flow of the pulse wave signal. (**b**) Confusion matrix resulting from data processing.

Fig. 9 | A snapshot of the smartphone application for monitored data visualization.

real-time pulse monitoring. Several commonly used algorithms for processing specklegrams were evaluated and compared to optimize the smart photonic wristband. The sum of squared differences (SSD) method showed the best performance, controlling the measurement error to approximately 4.9%. Subsequently, based on the SSD method, the POF with different core diameters was used for experimental investigation; the smart photonic wristband with POF (750 μm core diameter) had the highest signal-to-noise ratio and better sensitivity, corresponding to an SNR of 34.96 dB and a measurement delay of 369.9 ms between the smart photonic wristband measurement and the reference ECG signal, respectively, while the measurement error was reduced to 3.7%. Finally, the optimal processing algorithm and the smart photonic wristband were combined to obtain a set of methods suitable for long-term detection. The smart photonic wristband could monitor subtle changes in pulse wave characteristics, subsequently achieving wrist pulse measurements before and after exercise, as well as multiposition pulse detection. Future work will continue to focus on the Cunkou diagnostic method, refining the quantitative comparative analysis of pulse waves among various patients and healthy people. In addition, the AI algorithm has achieved the recognition of different gestures with 95% accuracy, which plays a vital role in screening potential patients with related diseases. Eventually, a cloud system was developed to monitor the user's pulse and exercise information and the data is interconnected using Wi-Fi to the cloud. Specifically, smart photonic wristbands have a wide range of potential applications in healthcare environments. We expect to deploy these in specific medical settings that demand resistance to electromagnetic interference, such as magnetic resonance imaging (MRI) systems, CT systems, and diagnostic ultrasound systems. The proposed sensor helps monitor pulse abnormalities caused by cardiovascular diseases, facilitates the integration of traditional Chinese pulse diagnosis with western medicine and these devices have the potential to be highly useful in the field of smart wearable physiological signal detection.

References

1. Chen SW, Qi JM, Fan SC et al. Flexible wearable sensors for cardiovascular health monitoring. *Adv Healthc Mater* **10**, 2100116 (2021).
2. Vogel B, Acevedo M, Appelman Y et al. The *Lancet* women and

cardiovascular disease commission: reducing the global burden by 2030. *Lancet* **397**, 2385–2438 (2021).
3. Gilgen-Ammann R, Schweizer T, Wyss T. RR interval signal quality of a heart rate monitor and an ECG Holter at rest and during exercise. *Eur J Appl Physiol* **119**, 1525–1532 (2019).
4. Zheng Q, Tang QZ, Wang ZL et al. Self-powered cardiovascular electronic devices and systems. *Nat Rev Cardiol* **18**, 7–21 (2021).
5. Tan PC, Xi Y, Chao SY et al. An artificial intelligence-enhanced blood pressure monitor wristband based on piezoelectric nanogenerator. *Biosensors* **12**, 234 (2022).
6. Chen SW, Wu N, Lin SZ et al. Hierarchical elastomer tuned self-powered pressure sensor for wearable multifunctional cardiovascular electronics. *Nano Energy* **70**, 104460 (2020).
7. Meng KY, Xiao X, Wei WX et al. Wearable pressure sensors for pulse wave monitoring. *Adv Mater* **34**, 2109357 (2022).
8. Chu Y, Zhong JW, Liu HL et al. Human pulse diagnosis for medical assessments using a wearable piezoelectret sensing system. *Adv Funct Mater* **28**, 1803413 (2018).
9. Sun YZ, Zhang ZQ, Zhou Y et al. Wearable strain sensor based on double-layer graphene fabrics for real-time, continuous acquirement of human pulse signal in daily activities. *Adv Mater Technol* **6**, 2001071 (2021).
10. Ouyang H, Tian JJ, Sun GL et al. Self-powered pulse sensor for antidiastole of cardiovascular disease. *Adv Mater* **29**, 1703456 (2017).
11. Wang SP, Wang XY, Wang S et al. Optical-nanofiber-enabled gesture-recognition wristband for human-machine interaction with the assistance of machine learning. *Adv Intell Syst* **5**, 2200412 (2023).
12. Chen GR, Au C, Chen J. Textile triboelectric nanogenerators for wearable pulse wave monitoring. *Trends Biotechnol* **39**, 1078–1092 (2021).
13. Roy K, Ghosh SK, Sultana A et al. A self-powered wearable pressure sensor and pyroelectric breathing sensor based on GO interfaced PVDF nanofibers. *ACS Appl Nano Mater* **2**, 2013–2025 (2019).
14. Yan C, Deng WL, Jin L et al. Epidermis-inspired ultrathin 3D cellular sensor array for self-powered biomedical monitoring. *ACS Appl Mater Interfaces* **10**, 41070–41075 (2018).
15. Zhu HH, Liu A, Luque HL et al. Perovskite and conjugated polymer wrapped semiconducting carbon nanotube hybrid films for high-performance transistors and phototransistors. *ACS Nano* **13**, 3971–3981 (2019).
16. Ma C, Xu D, Huang YC et al. Robust flexible pressure sensors made from conductive micropyramids for manipulation tasks. *ACS Nano* **14**, 12866–12876 (2020).
17. Wang S, Chen GR, Niu SY et al. Magnetic-assisted transparent and flexible percolative composite for highly sensitive piezoresistive sensor via hot embossing technology. *ACS Appl Mater Interfaces* **11**, 48331–48340 (2019).
18. Yang TT, Jiang X, Zhong YJ et al. A wearable and highly sensitive graphene strain sensor for precise home-based pulse wave monitoring. *ACS Sens* **2**, 967–974 (2017).
19. Xiong YX, Shen YK, Tian L et al. A flexible, ultra-highly sensitive and stable capacitive pressure sensor with convex microarrays for motion and health monitoring. *Nano Energy* **70**, 104436 (2020).
20. Guan FY, Xie Y, Wu HX et al. Silver nanowire-bacterial cellulose composite fiber-based sensor for highly sensitive detection of pressure and proximity. *ACS Nano* **14**, 15428–15439 (2020).
21. Lin QP, Huang J, Yang JL et al. Highly sensitive flexible iontronic pressure sensor for fingertip pulse monitoring. *Adv Healthc Mater* **9**, 2001023 (2020).
22. Min R, Liu ZY, Pereira L et al. Optical fiber sensing for marine environment and marine structural health monitoring: a review. *Opt Laser Technol* **140**, 107082 (2021).
23. Wang X, Zhou HY, Chen MH et al. Highly sensitive strain sensor based on microfiber coupler for wearable photonics healthcare. *Adv Intell Syst* **5**, 2200344 (2023).
24. Jia DG, Chao J, Li S et al. A fiber bragg grating sensor for radial artery pulse waveform measurement. *IEEE Trans Biomed Eng* **65**, 839–846 (2018).
25. Pant S, Umesh S, Asokan S. A novel approach to acquire the arterial pulse by finger plethysmography using fiber bragg grating sensor. *IEEE Sens J* **20**, 5921–5928 (2020).
26. Li HQ, An ZX, Zhang S et al. Fully photonic integrated wearable optical interrogator. *ACS Photonics* **8**, 3607–3618 (2021).
27. Li LY, Li YP, Yang LY et al. Continuous and accurate blood pressure monitoring based on wearable optical fiber wristband. *IEEE Sens J* **21**, 3049–3057 (2021).
28. Smith DL, Nguyen LV, Ottaway DJ et al. Machine learning for sensing with a multimode exposed core fiber specklegram sensor. *Opt Express* **30**, 10443–10455 (2022).
29. Murray MJ, Davis A, Kirkendall C et al. Speckle-based strain sensing in multimode fiber. *Opt Express* **27**, 28494–28506 (2019).
30. Gu LL, Gao H, Hu HF. Demonstration of a learning-empowered fiber specklegram sensor based on focused ion beam milling for refractive index sensing. *Nanomaterials* **13**, 768 (2023).
31. Chen W, Feng F, Chen DH et al. Precision non-contact displacement sensor based on the near-field characteristics of fiber specklegrams. *Sens Actuators A Phys* **296**, 1–6 (2019).
32. Qureshi MM, Liu Y, Mac KD et al. Quantitative blood flow estimation *in vivo* by optical speckle image velocimetry. *Optica* **8**, 1092–1101 (2021).
33. Bennett A, Beiderman Y, Agdarov S et al. Monitoring of vital biosigns by analysis of speckle patterns in a fabric-integrated multimode optical fiber sensor. *Opt Express* **28**, 20830–20844 (2020).
34. Min R, Hu XH, Pereira L et al. Polymer optical fiber for monitoring human physiological and body function: a comprehensive review on mechanisms, materials, and applications. *Opt Laser Technol* **147**, 107626 (2022).
35. Shi Y, Tangdiongga E, Koonen AMJ et al. Plastic-optical-fiber-based in-home optical networks. *IEEE Commun Mag* **52**, 186–193 (2014).
36. Talataisong W, Gorecki J, van Putten LD et al. Hollow-core antiresonant terahertz fiber-based TOPAS extruded from a 3D printer using a metal 3D printed nozzle. *Photonics Res* **9**, 1513–1521 (2021).
37. Woyessa G, Fasano A, Markos C et al. Zeonex microstructured polymer optical fiber: fabrication friendly fibers for high temperature and humidity insensitive Bragg grating sensing. *Opt Mater Express* **7**, 286–295 (2017).
38. Theodosiou A, Min R, Leal-Junior AG et al. Long period grating in a multimode cyclic transparent optical polymer fiber inscribed using a femtosecond laser. *Opt Lett* **44**, 5346–5349 (2019).
39. Liu L, Zheng J, Deng SJ et al. Parallel polished plastic optical fiber-based SPR sensor for simultaneous measurement of RI

and temperature. *IEEE Trans Instrum Meas* **70**, 9508308 (2021).
40. Leal-Junior AG, Frizera A, Marques C et al. Optical fiber specklegram sensors for mechanical measurements: a review. *IEEE Sens J* **20**, 569–576 (2020).
41. Avellar L, Delgado G, Marques C et al. Polymer optical fiber-based smart garment for impact identification and balance assessment. *IEEE Sens J* **21**, 20078–20085 (2021).
42. Cooley JW, Lewis PAW, Welch PD. The fast Fourier transform and its applications. *IEEE Trans Ed* **12**, 27–34 (1969).
43. Jokinen H, Ollila J, Aumala O. On windowing effects in estimating averaged periodograms of noisy signals. *Measurement* **28**, 197–207 (2000).
44. Di Stefano L, Mattoccia S, Tombari F. ZNCC-based template matching using bounded partial correlation. *Pattern Recognit Lett* **26**, 2129–2134 (2005).
45. Kumar CK, Manaswini M, Maruthy KN et al. Association of Heart rate variability measured by RR interval from ECG and pulse to pulse interval from photoplethysmography. *Clin Epidemiol Global Health* **10**, 100698 (2021).
46. Quer G, Gouda P, Galarnyk M et al. Inter- and intraindividual variability in daily resting heart rate and its associations with age, sex, sleep, BMI, and time of year: retrospective, longitudinal cohort study of 92, 457 adults. *PLoS One* **15**, e0227709 (2020).
47. Neha, Sardana HK, Kanwade R, Tewary S. Arrhythmia detection and classification using ECG and PPG techniques: a review. *Phys Eng Sci Med* **44**, 1027–1048 (2021).
48. Rodríguez-Cuevas A, Peña ER, Rodríguez-Cobo L et al. Low-cost fiber specklegram sensor for noncontact continuous patient monitoring. *J Biomed Opt* **22**, 037001 (2017).
49. Hill KO, Tremblay Y, Kawasaki BS. Modal noise in multimode fiber links: theory and experiment. *Opt Lett* **5**, 270–272 (1980).
50. Wang J, Zhu YR, Wu ZY et al. Wearable multichannel pulse condition monitoring system based on flexible pressure sensor arrays. *Microsyst Nanoeng* **8**, 16 (2022).
51. Tyan CC, Liang WM, Shy HY et al. How to standardize 3 finger positions of examiner for palpating radial pulses at wrist in traditional Chinese medicine. *Acupunct Electrother Res* **32**, 87–96 (2007).

Acknowledgements

We are grateful for financial supports from National Key R&D Program of China (2022YFE0140400), National Natural Science Foundation of China (62003046, 62111530238), Guangdong Basic and Applied Basic Research Foundation (2021A1515011997), The Supplemental Funds for Major Scientific Research Projects of Beijing Normal University, Zhuhai (ZHPT2023007), Special project in key field of Guangdong Provincial Department of Education (2021ZDZX1050) and The Innovation Team Project of Guangdong Provincial Department of Education (2021KCXTD014). Fundação para a Ciência e a Tecnologia (FCT) through the 2021.00667. CEECIND (iAqua project) and PTDC/EEI-EEE/0415/2021 (DigiAqua project); The project i3N, UIDB/50025/2020 n& UIDP/50025/2020, financed by national funds through the FCT/MEC.

Author contributions

RF Kuang, R Min conceived the project idea and designed the experiments. RF Kuang, Z Wang, L Ma, H Wang, and QM Chen carried out the experiments and collected the data. K. R., and H Wang contributed to sensor fabrication and cardiorespiratory monitoring experiment. Z Wang, L Ma, A Leal Junior, and C Marques contributed to behaviour monitoring experiment. RF Kuang, R Min, A Leal Junior, S Kumar, X Li and C Marques analysed all the data and cowrote the paper. All authors discussed the results and commented on the manuscript.

Competing interests

The authors declare no competing financial interests.

Supplementary information

Supplementary information for this paper is available at https://doi.org/10.29026/oes.2024.240009

Scan for Article PDF